Nanoscale Research Letters

NANO EXPRESS

Open Access

CrossMark

Preparation of PPy-Coated MnO_2 Hybrid Micromaterials and Their Improved Cyclic Performance as Anode for Lithium-Ion Batteries

Lili Feng[1,2]* iD, Yinyin Zhang[1,2], Rui Wang[1,2], Yanli Zhang[1,2], Wei Bai[1,2], Siping Ji[1,2], Zhewen Xuan[1,2], Jianhua Yang[1,2], Ziguang Zheng[1,2] and Hongjin Guan[1,2]

Abstract

MnO_2@PPy core-shell micromaterials are prepared by chemical polymerization of pyrrole on the MnO_2 surface. The polypyrrole (PPy) is formed as a homogeneous organic shell on the MnO_2 surface. The thickness of PPy shell can be adjusted by the usage of pyrrole. The analysis of SEM, FT-IR, X-ray photoelectron spectroscopy (XPS), thermogravimetric analysis (TGA), and XRD are used to confirm the formation of PPy shell. Galvanostatic cell cycling and electrochemical impedance spectroscopy (EIS) are used to evaluate the electrochemical performance as anode for lithium-ion batteries. The results show that after formation of MnO_2@PPy core-shell micromaterials, the cyclic performance as anode for lithium-ion batteries is improved. Fifty microliters of PPy-coated caddice-clew-like MnO_2 has the best cyclic performances as has 620 mAh g^{-1} discharge specific capacities after 300 cycles. As a comparison, the discharge specific capacity of bare MnO_2 materials falls to below 200 mAh g^{-1} after 10 cycles. The improved lithium-storage cyclic stability of the MnO_2@PPy samples attributes to the core-shell hybrid structure which can buffer the structural expansion and contraction of MnO_2 caused by the repeated embedding and disengagement of Li ions and can prevent the pulverization of MnO_2. This experiment provides an effective way to mitigate the problem of capacity fading of the transition metal oxide materials as anode materials for (lithium-ion batteries) LIBs.

Keywords: Manganese dioxide, PPy, Lithium-ion battery, Anode material

Background

Since 3d transition metal oxides (MO; where M is Fe, Co, Ni, and Cu) were proposed to serve as high theoretic capacity anodes for lithium-ion batteries by Tarascon et al. [1], many efforts have been made in preparing micro/nano-metal oxides with various morphologies and researching their electrochemical performance as anode for lithium-ion batteries [2–6]. For examples, Zhu's research group had made monodisperse Fe_3O_4 and γ-Fe_2O_3 microspheres via a surfactant-free solvothermal method [3]. They had a high initial discharge capacity of 1307 and 1453 mAh g^{-1}, respectively. After 110 cycles, the discharge capacity remained at 450 mAh g^{-1} for Fe_3O_4 and 697 mAh g^{-1} for γ-Fe_2O_3. Hongjing Wu et al. had prepared uniform multi-shelled especially quintuple-shelled NiO hollow spheres by a simple shell-by-shell self-assembly hydrothermal treatment. The merit of this research made a significant contribution to the synthetic methodology of multi-shelled hollow structures. But the lithium storage performances of the NiO hollow spheres were not very excellent [4]. MnO_2 possess high theoretically gravimetric lithium storage capacity of about 1230 mAh g^{-1}; therefore, many researches are made to the design, synthesis, and applications of MnO_2 anodes for lithium-ion battery [7–10]. For instance, Chen's research group had made γ-MnO_2 with hollow microspherical shape and nanocubic shape [11].

* Correspondence: lilylian2003@163.com
[1]School of Chemistry and Environment, Yunnan Minzu University, Kunming 650500, China
[2]Key Laboratory of Resource Clean Conversion in Ethnic Regions, Education Department of Yunnan, Yunnan Minzu University, Kunming 650500, China

Feng et al. Nanoscale Research Letters (2017) 12:518

Page 2 of 10

After 20 cycles, the discharge capacities of the nano-cubes and microspheres were 656.5 and 602.1 mAh g^{-1}. In addition, they had made many researches on MnO_2 materials for lithium-ion battery from the year 2000 to now [12, 13]. We also studied the applications of MnO_2 anodes for lithium-ion battery, but the discharge specific capacity of bare MnO_2 materials felled so fast to below 200 mAh g^{-1} after 10 cycles [14].

Although transition metal oxides materials have large theoretical specific capacities, all these materials including MnO_2 anodes are generally plagued by rapid capacity fading. The reasons for the poor cycling stability are as follows: (1) the electronic conductivity of transition metal oxides materials are usually low, and the electron or ion have difficulties in the diffusion process, resulting in irreversible electrode reaction and fast capacity decay. (2) After charge/discharge cycles, transition metal oxides suffer from enormous mechanical stress and pulverize, leading to electrical contact loss between active particles and current collector. The transition metal oxide particles without electrical contact can no longer participate in the charge/discharge cycles, resulting in capacity fading [15, 16].

Shell coating is an effective strategy to improve the cycling stability. In this structure, to a certain extent, the shell can buffer the structural expansion and contraction of metal oxide materials caused by the repeated embedding and disengagement of the Li ions. For the moment, carbon coating, organic conducting polymer coating, graphene hybrid, and other inorganic compound coating have been used [17, 18]. For instance, Yin et al. prepared polypyrrole (PPy)-coated CuO nanocomposites. The core-shell sample had a high reversible capacity of 760 mAh g^{-1} which was much better than those of the bare CuO sample [19]. Li et al. prepared graphene-wrapped MnO_2 nanoribbons. The reversible specific discharge capacity reached 890 mAh g^{-1} at 0.1 A g^{-1} after 180 cycles. Therefore, it is necessary and urgent to make PPy shell coating on MnO_2 materials to improve the cyclic stability as anode for lithium-ion batteries [20].

In the present work, to improve the cyclic performance of MnO_2 materials as anode for lithium-ion batteries, polypyrrole (an organic conducting polymer) coating had been prepared by chemical polymerization. As a result, the cyclic performance was improved after formation of MnO_2@PPy core-shell micromaterials. This experiment provides an effective way to mitigate the problem of capacity fading of the transition metal oxides materials as anode materials for (lithium-ion batteries) LIBs.

Methods
Preparation of Samples
All reagents were of analytical grade and purchased from the Shanghai Chemical Company. The pyrrole was purified by decompressional distillation prior to use and stored at 0–5 °C and guarded against exposure to light to prevent residual polymerization. Other reagents were used without further purification.

The MnO_2 micromaterials were prepared using the similar method described by Yu et al. [14, 21] as some modification. To prepare caddice-clew-like MnO_2 micromaterial, 1.70 g $MnSO_4 \cdot H_2O$ was dissolved in 15 mL distilled water with vigorous stirring. When the solution was clear, 20 mL aqueous solution containing 2.72 g $K_2S_2O_8$ were added to the above solution under continuous stirring. Then, the resulting transparent solution was transferred into a Teflon-lined stainless steel autoclave (50 mL) of 80% capacity of the total volume. The autoclave was sealed and maintained at 110 °C for 6 h. After the reaction was completed, the autoclave was allowed to cool to room temperature naturally. The solid black precipitate was filtered, washed several times with distilled water to remove impurities, and then dried at 80 °C in air for 3 h. The obtained caddice-clew-like MnO_2 micromaterial was collected for the fabrication of PPy-coated MnO_2 materials. Urchin-like MnO_2 micromaterial was prepared by the similar method; after adding 1.70 g $MnSO_4 \cdot H_2O$ and 2.72 g $K_2S_2O_8$ into 35 mL distilled water, 2 mL H_2SO_4 was then added.

The MnO_2@PPy hybrid micromaterials were prepared by chemical polymerization of pyrrole on the MnO_2 surface using sodium benzenesulfonate (BSNa) as surfactant and $FeCl_3$ as oxidant. The molar ratio of monomer pyrrole to BSNa was 3:1. First, 0.2 g MnO_2 was dispersed into a beaker containing 50 mL of 0.01 mol L^{-1} BSNa aqueous solution and stirred for 0.5 h. The mixture was put in an ice/water bath (0–5 °C) under stirring. Then, a certain amount of pyrrole was added to the mixture. After stirring for 0.5 h, a small amount of $FeCl_3$ solution was dropwise added into the aqueous solution to start the polymerization process. The gradual change of color from light black to deep black indicated the formation of PPy. The mixture was kept at 0–5 °C under stirring for 12 h to form MnO_2@PPy core-shell micromaterials. The thickness of PPy was controlled by pyrrole usage. Finally, the obtained composite was filtered, washed with water and ethanol, and then dried under vacuum at 60 °C for 4 h.

Characterization of Samples
The morphological investigations of SEM images and energy dispersive spectroscopy (EDS) were taken on a scanning electron microscope (QUANTA-200 America FEI Company). The crystallographic structures of the products were determined with XRD which were recorded on a Rigaku D/max-2200/PC with Cu target at a scanning rate of 7°/min with 2θ ranging from 10° to 70°. Fourier transform infrared (FT-IR) spectra of the MnO_2@PPy hybrid micromaterials palletized with KBr

Feng *et al. Nanoscale Research Letters* (2017) 12:518

Page 3 of 10

were performed on a Nicolet IS10 spectrometer. Thermo-gravimetric analysis (TGA) was also used to determine the weight loss of MnO_2@PPy hybrid micromaterials at 10 °C/min from 25 to 800 °C in air (MELER/1600H Thermogravimetric Analyzer). X-ray photoelectron spectroscopy (XPS) measurements were recorded on a Ulvac-PHI, PHI5000 Versaprobe-II X-ray photoelectron spectroscope, using Al Kα X-rays as the excitation source. The binding energy obtained in the XPS analysis was calibrated against the C1s peak at 284.8 eV.

Cell Assembly and Electrochemical Studies

Electrochemical lithium-storage properties of the synthesized products were measured by using CR2025 coin-type test cells assembled in a dry argon-filled glove box. To fabricate the working electrode, a slurry consisting of 60 wt.% active materials, 10 wt.% acetylene black, and 30 wt.% poly-vinylidene fluoride (PVDF) dissolved in *N*-methyl pyrrolidinone was casted on a copper foil, dried at 80 °C under vacuum for 5 h. A lithium sheet was served as counter and reference electrode, while a Celgard 2320 membrane was employed as a separator. The electrolyte was a solution of 1 M $LiPF_6$ in ethylene carbonate (EC)-1,2-dimethyl carbonate (DMC) (1:1 in volume). Galvanostatical charge-discharge experiments were performed by Land electric test system CT2001A (Wuhan Land Electronics Co., Ltd.) at a current density of 0.2 C between 0.01 and 3.00 V (versus Li/Li$^+$). When calculating the specific capacity of MnO_2@PPy core-shell micromaterials, the mass of PPy was included. Electrochemical impedance spectroscopy (EIS) measurements were performed on an electrochemical workstation (CHI604D, Chenhua, Shanghai), and the frequency ranged from 0.1 Hz to 100 KHz with an applied AC signal amplitude of 5 mV.

Results and Discussion

Morphological Features of Samples

The morphologies of pure PPy sample, sea-urchin-like MnO_2 sample, and the MnO_2@PPy hybrid micromaterials with different pyrrole polymerization amount are characterized by SEM measurements. As shown in Fig. 1, the pure PPy sample has a sphere shape with about 800 nm in diameter and tends to agglomerate together as layered rocks. The urchin-like MnO_2 sample is shown in Fig. 1a. The MnO_2 micromaterial is a uniform sea-urchin-like shape with a diameter of approximately 3 μm, which consists of several straight and radially grown nanorods with uniform length of about 1 μm. The evolution of the morphologies of MnO_2@PPy hybrid micromaterials is shown in Fig.1b–e. When the amount of pyrrole is small, the PPy first nucleates and then embeds into the gap of needle-like nanorods of MnO_2 samples. The needle-like nanorods in Fig. 1b are
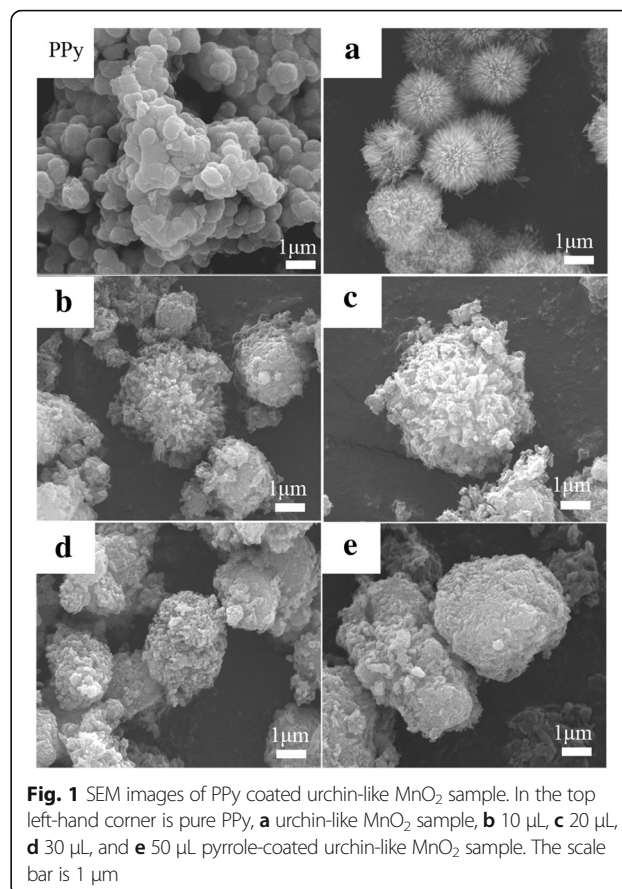

Fig. 1 SEM images of PPy coated urchin-like MnO_2 sample. In the top left-hand corner is pure PPy, **a** urchin-like MnO_2 sample, **b** 10 μL, **c** 20 μL, **d** 30 μL, and **e** 50 μL pyrrole-coated urchin-like MnO_2 sample. The scale bar is 1 μm

obviously wider than those showed in Fig. 1a. When the amount of pyrrole increases to 20 μL, the nanorod structure still exists but not obvious. As pyrrole quantity increases to 30 μL, the needle-like nanorod structure of MnO_2 micromaterials disappears completely and become spherical in shape. When pyrrole quantity further increases (Fig. 1e), the PPy shell becomes very thick. Scheme 1 illustrates the possible formation processes for the MnO_2@PPy hybrid micromaterials. In the first stage, a tiny crystal nucleus of PPy generates from monomer pyrrole by the oxidation of $FeCl_3$. Then, the crystal nucleus deposits into the gap between the thorns on the surface of the "urchin." With the continuous polymerization of PPy, the gap between the thorns is gradually filled up. At the end, the whole "urchin" is uniformly coated by PPy. The low magnification SEM images of MnO_2@PPy hybrid micromaterials in Additional file 1 confirm that PPy shell is formed uniformly on MnO_2@PPy sample.

In this work, caddice-clew-like MnO_2 micromaterial is also coated by PPy using the similar method. The SEM morphologies are shown in Additional file 1: Supporting information 1. The caddice-clew-like MnO_2 micromaterial is nanowire shaped and aggregates into 2–4 μm diameter spheres which look like a caddice-clew. When

Feng *et al. Nanoscale Research Letters* (2017) 12:518

Page 4 of 10
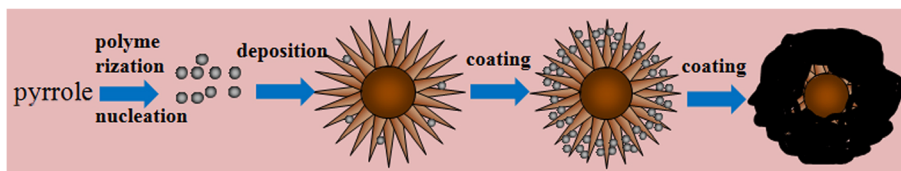
Scheme 1 Schematic illustration of the formation mechanism proposed for MnO$_2$@PPy material

the amount of pyrrole is small, the PPy first forms as small particles and adheres on the surface of the MnO$_2$ samples. With the amount of pyrrole increasing, PPy gradually cover the caddice-clew-like MnO$_2$ completely to form a large block structure which looks like rocks.

The uniform coating of PPy is further verified by energy-dispersive X-ray (EDX) spectroscopy analysis (shown in Table 1). No carbon and nitrogen signals are detected on pure MnO$_2$ sample. Significant amount of carbon and nitrogen signals are detected on PPy and MnO$_2$@PPy samples due to the formation of the PPy shell. With increasing pyrrole usage, the content of carbon and nitrogen are also increased. The EDX data of caddice-clew-like MnO$_2$@PPy samples are shown in Additional file 1: Supporting Information 4.

FT–IR Analysis of Samples

The structure features and compositions of the synthesized PPy and MnO$_2$@PPy samples are further characterized by FT-IR spectroscopy (shown in Fig. 2). For all the MnO$_2$@ PPy samples and PPy sample, the bands at 1550, 1448, 1283, and 1130 cm^{-1} are the characteristic peaks of the PPy rings. Among them, the peak at about 1550 cm^{-1} is due to C-C and C=C stretching, and the peak at about 1448 cm^{-1} is from C-N stretching of PPy. The peak at about 1130 cm^{-1} is due to the S=O stretching vibration peak that belongs to the BSNa, which indicates that the sulfonate ion is doped into the pyrrole ring. The ratio of I_{1550} and I_{1448} is usually ascribed to the conjugate and the doping degree of the PPy [22]. The higher the I_{1550}/I_{1448} is the higher conjugate and doping degree of PPy is. That is, if I_{1550}/I_{1448} is high, the conductivity of PPy should be better. The bands at 1550, 917, and 778 cm^{-1} of 30 μL PPy-coated urchin-like MnO$_2$ sample are weaker than those of 50 μL PPy-coated caddice-clew-like MnO$_2$ sample. So, the conductivity of PPy-coated caddice-clew-like MnO$_2$ sample
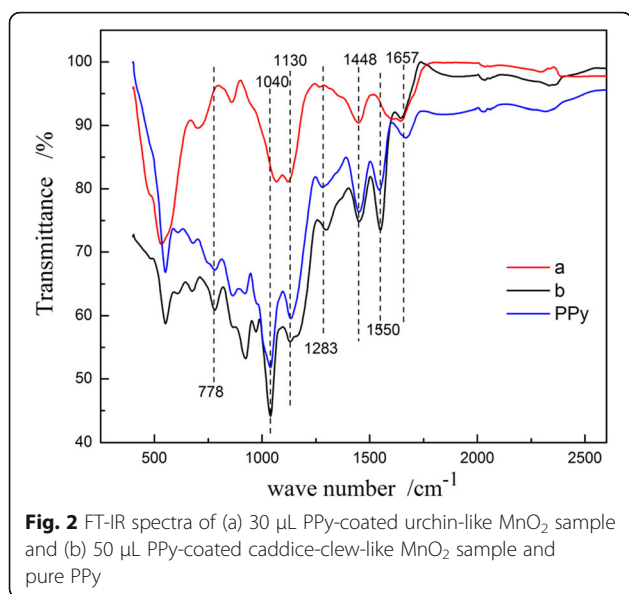
should be better, and the 50 μL PPy-coated caddice-clew-like MnO$_2$ sample should have better lithium-storage performance. Bands at 1040 and 778 cm^{-1} are the in-plane and out-of-plane vibrations of C-H deformation of C_β-H absorption band. No C_α-H absorption band is observed in the spectrum, which indicates that the pyrrole ring is predominantly linked by α-α in PPy. The absorption band at 1657 cm^{-1} is due to the existence of water molecules in the products. Therefore, the FT-IR results prove that PPy shell is formed on MnO$_2$@PPy sample.

XPS Results

Usually, core-shell structure should be verified by TEM. However, the pure MnO$_2$ sample here is too thick to take good TEM images. So, to verify the core-shell structure, we did XPS test and EDS test to verify the different components in the surface and the whole sample. For clarity, only the spectroscopy of 30 μL PPy-coated urchin-like MnO$_2$ sample and 50 μL PPy-coated caddice-clew-like MnO$_2$ sample are shown in Fig. 3. Others are in the Additional file 1: Supporting Information 5. The final results are listed in Table 2. The main binding energies (BE) of O1s, N1s, C1s, and Mn(2p1/2, 2p3/2) are determined to be 531.2, 398.9, 284.8 and 651.4 and 640.3 eV, respectively. The peaks at 973 and 901.6, and 848.9 eV are O KLL peaks (Auger peaks from oxygen atoms) and Mn LMM peaks (Auger peaks from Mn atoms). There is a few Fe or Cl detected by XPS, shown in Fig. 3. Here, the appearance of Fe or Cl signals is due to the use of FeCl$_3$ as polymerization oxidant in preparing PPy shell. As can be seen in Table 2, the differences of EDS analysis and XPS analysis are distinct. In XPS analysis, the content of O, N, and C are much higher; the content of Mn is lower. The max analysis depth of XPS is about 5–10 nm. The strong O, N, and C peaks confirm that the MnO$_2$ samples are covered by

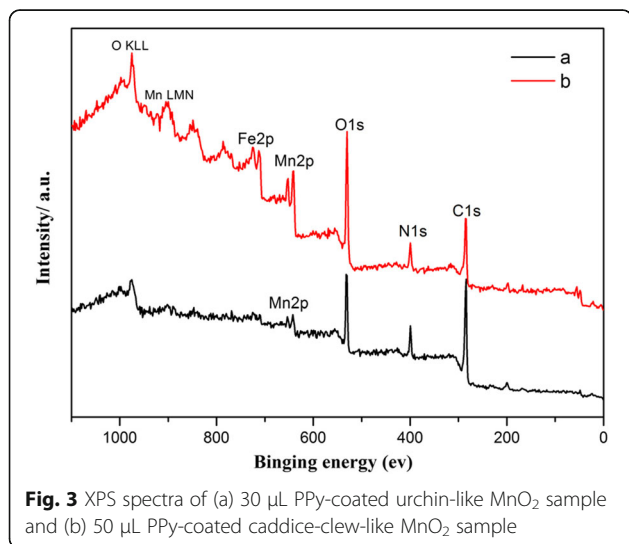**Table 1** EDX data for PPy, MnO$_2$, and PPy-coated urchin-like MnO$_2$ sample

Element	PPy At%	MnO$_2$ At%	MnO$_2$@PPy(10 μL) At%	MnO$_2$@PPy(20 μL) At%	MnO$_2$@PPy(30 μL) At%	MnO$_2$@PPy(50 μL) At%
C	62.99	–	13.78	06.51	35.11	21.50
N	19.03	–	04.94	04.62	09.64	07.03
O	10.13	34.02	36.57	36.53	22.27	30.06
Mn	–	65.98	44.71	38.84	18.23	28.35

Feng *et al. Nanoscale Research Letters* (2017) 12:518

Page 5 of 10

Fig. 2 FT-IR spectra of (a) 30 μL PPy-coated urchin-like MnO_2 sample and (b) 50 μL PPy-coated caddice-clew-like MnO_2 sample and pure PPy

the PPy organic film (as described in the SEM paragraph).

TGA Results

To prove the PPy shell on the synthesized MnO_2@PPy samples, TGA of bare MnO_2 sample, bare PPy, and MnO_2@PPy samples are carried out in air. Figure 4 is the TGA results. As can be seen from Fig. 4, the bare PPy powder displays two weight loss regions. The first weight loss about 12% in the temperature range of 60–260 °C can be attributed to the desorption of physisorbed water and removal of surface-absorbed solvents as mentioned in the previous literatures [19, 23, 24]. While the second weight loss about 88% in the range of 260–600 °C is ascribed to the oxidation of PPy. As a result, bare PPy powder is thoroughly burn off at 600 °C.

Fig. 3 XPS spectra of (a) 30 μL PPy-coated urchin-like MnO_2 sample and (b) 50 μL PPy-coated caddice-clew-like MnO_2 sample

After TGA test, the bare urchin-like MnO_2 sample and caddice-clew-like MnO_2 sample remain 88.7wt.% and 91.6% at 800 °C. The most weight loss is in the temperature range of 60–300 °C, so it can be ascribed to the removal of surface absorbed solvents, although both samples looked very dry. For 30 μL PPy-coated urchin-like MnO_2 sample, the weight loss in the range of 60–260 °C is 10%, and the whole weight loss in the range of 0–800 °C is 32.3%. The change in weight before and after the oxidation of PPy can be directly translated into the amount of PPy in the MnO_2@PPy sample [25]. Using this method, the amounts of PPy in the 30 μL PPy-coated urchin-like MnO_2 sample is about 22%. This value is close to the theoretical amounts of PPy. For 50 μL PPy-coated caddice-clew-like MnO_2 sample, the whole weight loss in the range of 0–800 °C is 43.9% and the weight loss in the range of 60–260 °C is 14%. So, the actual amounts of PPy in 50 μL PPy-coated caddice-clew-like MnO_2 sample is about 30% which is much near to the theoretical value. Therefore, the results confirm that the MnO_2 particles are covered by the PPy organic film.

XRD Characterization of Samples

The crystalline structures of MnO_2@PPy samples are examined by XRD (Fig. 5). As shown, PPy is an amorphous structure. When coated by PPy, the urchin-like MnO_2@PPy samples retain the α-MnO_2 structure. The diffraction peaks appear at 2θ = 12.7°, 18.1°, 28.8°, 37.5°, 42.1°, 49.9°, 56.2°, and 60.3° match well with the diffraction peaks of (110),(200),(310),(211),(301),(411),(600), and (521) crystal planes of α-MnO_2 standard data (JCPDS card PDF file No. 44-0141). With the increasing of the amount of PPy, the intensity of XRD peaks decrease gradually due to the formation of amorphous PPy. As shown in the PPy-coated caddice-clew-like MnO_2 samples, there are obvious amorphous peaks from 15° to 30° in 75 and 100uL samples. When coated by PPy, the caddice-clew-like MnO_2@PPy samples retain α-MnO_2 structure too. With the increasing of the amount of PPy, the materials obviously change from crystalline to amorphous. These results further prove that the PPy organic film have successfully coated on MnO_2 particles.

Electrochemical Performance

The electrochemical performances of these MnO_2@PPy samples as anode materials for LIBs are investigated. Figure 6a, b present the typical charge-discharge curves of the anodes (compared to the full battery) constructed from the bare MnO_2 sample and MnO_2@PPy samples at 0.2 C rate in the voltage range of 0.01−3.00 V (vs. Li/Li$^+$). For clarity, only the bare MnO_2 sample and the MnO_2@PPy with the best charge-discharge performances are shown. As can be seen, the discharge-charge

Feng *et al. Nanoscale Research Letters* (2017) 12:518

Page 6 of 10

Table 2 XPS data for urchin-like MnO$_2$@PPy sample

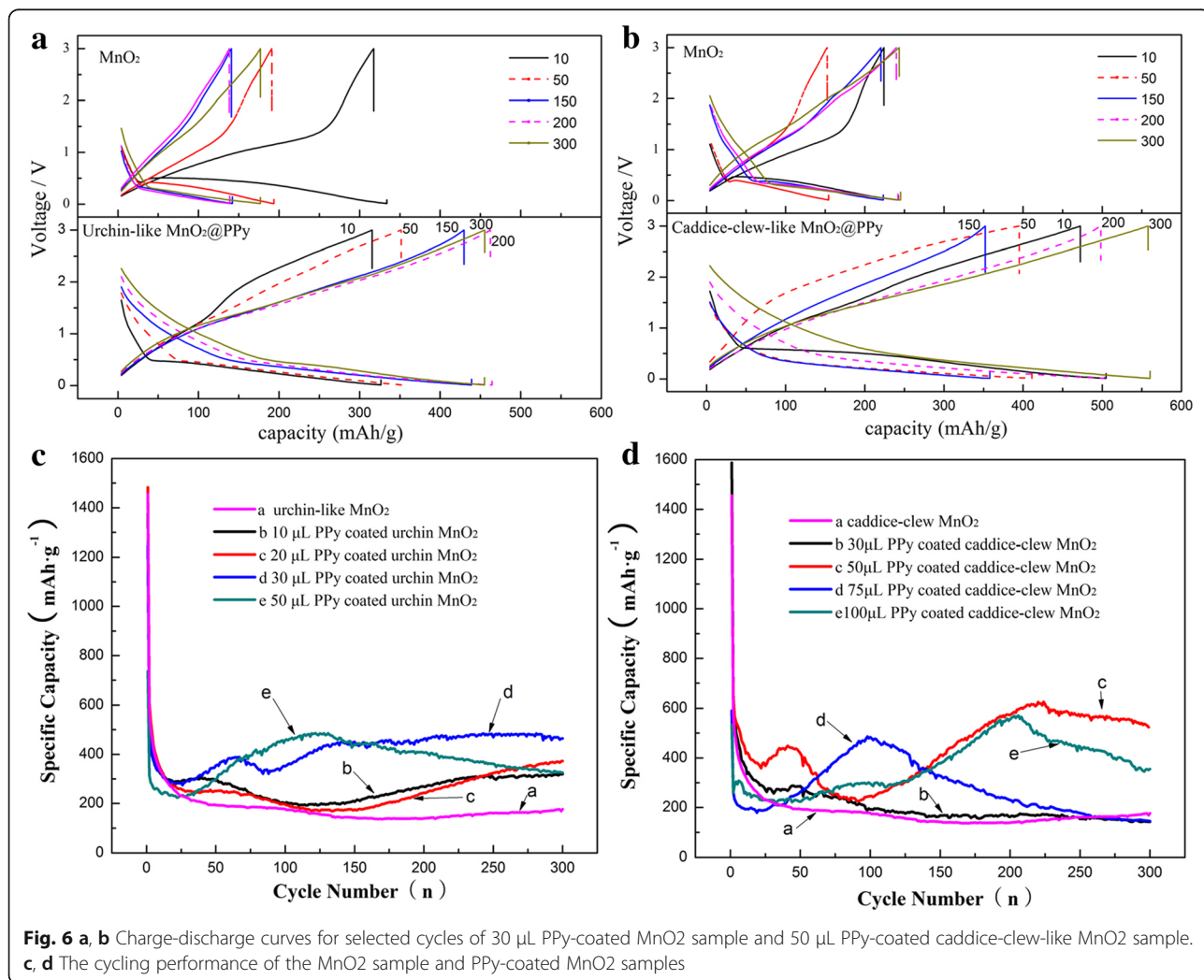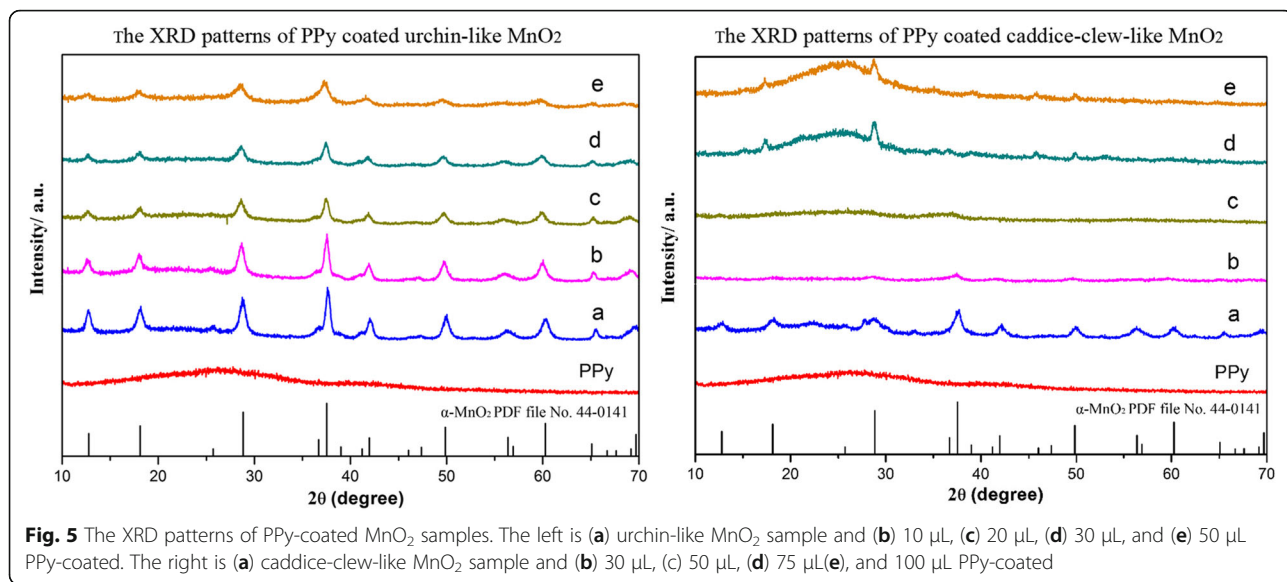| Element	MnO$_2$@PPy(10 µL) At%		MnO$_2$@PPy(30 µL)At%		MnO$_2$@PPy(50 µL)At%	
	EDX	XPS	EDX	XPS	EDX	XPS
C	07.39	49.1	35.11	65.8	21.50	69.4
N	–	1.30	09.64	11.0	07.03	12.8
O	16.24	46.8	22.27	22.0	30.06	16.4
Mn	13.61	2.90	18.23	0.50	28.35	1.10

profiles of MnO$_2$@PPy samples are similar to those of bare MnO$_2$, which indicates that the hybrid products coated by organic PPy shells do not change the electrochemical nature of MnO$_2$ LIBs anodes. However, the lithium storage performance of PPy-coated MnO$_2$ sample has been improved greatly. The bare urchin-like MnO$_2$ sample and PPy-coated urchin-like MnO$_2$ sample both have high initial discharge specific capacity as approximate 1200–1400 mAh g^{-1}, while the theoretical discharge specific capacity is 1232 mAh g^{-1}. The extra discharge specific capacities may result from the formation of SEI layer [14]. After 10 cycles, the discharge specific capacity of bare urchin-like MnO$_2$ sample decreases to below 200 mAh g^{-1}. As a comparison, the discharge specific capacity of PPy-coated urchin-like MnO$_2$ sample remains at about 500 mAh g^{-1} even after 300 cycles. The caddice-clew-like MnO$_2$ and the PPy-coated caddice-clew-like MnO$_2$ are much similar. After 10 cycles, the discharge specific capacity of bare caddice-clew-like MnO$_2$ decreases to below 200 mAh g^{-1}. The PPy-coated caddice-clew-like MnO$_2$ sample maintains at 500–600 mAh g^{-1} after 300 cycles.
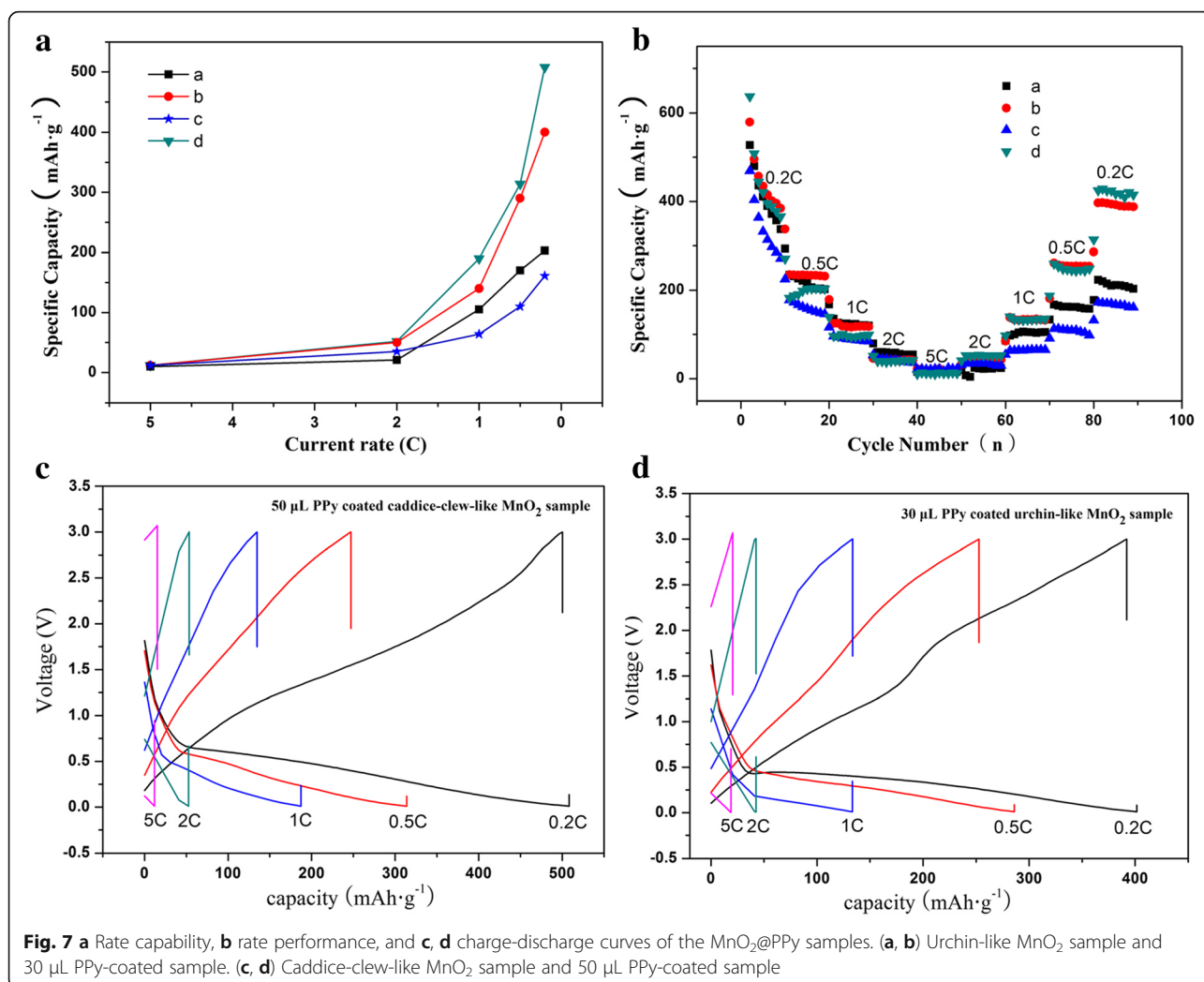
To evaluate their lithium-storage cyclic stability, discharge/charge measurements are performed for 300 cycles on MnO$_2$@PPy samples with different pyrroles coated. The thickness of PPy is controlled by the amount

Fig. 4 TGA curves of PPy and MnO$_2$ samples. (**a**) urchin-like MnO$_2$ sample, (**b**) caddice-clew-like MnO$_2$ sample, (**c**) 30 µL PPy-coated urchin-like MnO$_2$ sample, and (**d**) 50 µL PPy-coated caddice-clew-like MnO$_2$ sample

of pyrrole. As shown in Fig. 6c, d, when the amount of pyrrole is small (such as 30 uL for caddice-clew-like MnO$_2$ and 10 uL for urchin-like MnO$_2$), the lithium-storage capacity of this hybrid MnO$_2$@PPy sample improves not clearly. This indicates that the PPy film is too thin to prevent MnO$_2$ materials suffering from pulverization. However, when the amount of pyrrole increases, the discharge specific capacities of hybrid MnO$_2$@PPy samples are remarkably enhanced. For caddice-clew-like MnO$_2$, when the amount of pyrrole increases to 50 uL, the hybrid MnO$_2$@PPy sample has the biggest discharge specific capacities as 620 mAh g^{-1} after 300 cycles. For urchin-like MnO$_2$, the biggest discharge specific capacity appears when 30 uL pyrrole is used. The discharge specific capacity at the 300th cycle is 480 mAh g^{-1}. Furthermore, as can be seen from Fig. 6c, d, all the hybrid MnO$_2$@PPy samples have improved cyclic stabilities. The improved lithium-storage cyclic stabilities of the hybrid MnO$_2$@PPy samples can attribute to the unique structure of the metal oxide/conducting polymer core-shell hybrid products. In this structure, the flexible PPy shell can effectively buffer the structural expansion and contraction of MnO$_2$ caused by the repeated embedding and disengagement of the Li ions. In addition, the PPy shell can prevent the pulverization of MnO$_2$, as well as protect the loss of electrical contact between the MnO$_2$ material and the current collector (copper foil). Whereas, the low capacity and fast capacity fading of bare MnO$_2$ can attribute to the pulverization and loss of inter-particle contact of MnO$_2$ or the contact of MnO$_2$ with copper foil collector due to large volume expansion/contraction during repeated charging-discharging processes. Therefore, this experiment of PPy coating provides an effective way to mitigate the problem of capacity fading of all the transition metal oxide materials as anode materials for LIBs.

The rate performance of MnO$_2$@PPy samples are shown in Fig. 7. To test the rate capability, charge/discharge cycles are performed at the voltage range of 0.01–3.0 V and the discharge rate as 0.2C → 0.5C → 1.0C → 2.0C → 5.0C → 2.0 C → 1.0 C → 0.5C → 0.2C. Figure 7a is the rate capability in the stage from 5.0 to 0.2 C. As shown, the discharge specific capacity of all the MnO$_2$ samples in the 5.0 to 0.2 C stage is much similar to that in the stage from 0.2 to 5 C, which proofs that the MnO$_2$ samples have relatively high
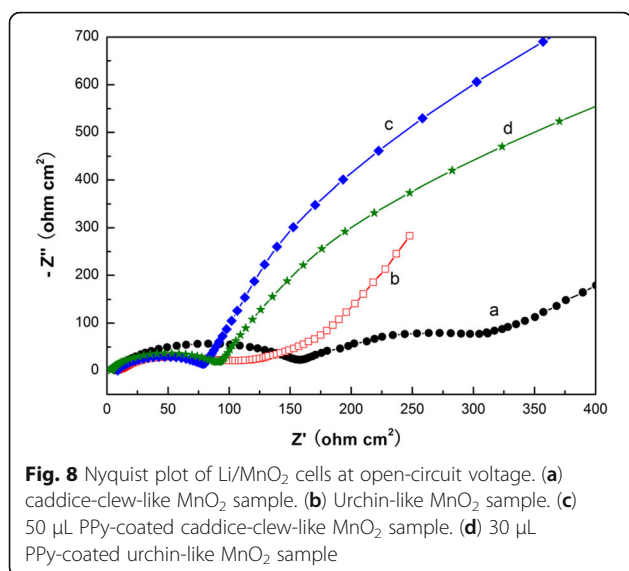
Feng *et al. Nanoscale Research Letters* (2017) 12:518

Page 7 of 10

Fig. 5 The XRD patterns of PPy-coated MnO₂ samples. The left is (**a**) urchin-like MnO₂ sample and (**b**) 10 μL, (**c**) 20 μL, (**d**) 30 μL, and (**e**) 50 μL PPy-coated. The right is (**a**) caddice-clew-like MnO₂ sample and (**b**) 30 μL, (**c**) 50 μL, (**d**) 75 μL(**e**), and 100 μL PPy-coated

Fig. 6 a, **b** Charge-discharge curves for selected cycles of 30 μL PPy-coated MnO2 sample and 50 μL PPy-coated caddice-clew-like MnO2 sample. **c**, **d** The cycling performance of the MnO2 sample and PPy-coated MnO2 samples

Feng *et al. Nanoscale Research Letters* (2017) 12:518

Page 8 of 10

Fig. 7 a Rate capability, **b** rate performance, and **c**, **d** charge-discharge curves of the MnO$_2$@PPy samples. (**a**, **b**) Urchin-like MnO$_2$ sample and 30 μL PPy-coated sample. (**c**, **d**) Caddice-clew-like MnO$_2$ sample and 50 μL PPy-coated sample

reversibility. However, the discharge specific capacities of all the MnO$_2$ samples are poor above the 1 C rate. The merit of the hybrid MnO$_2$@PPy samples in the rate performance can be seen at the low rates (0.2, 0.5, and 1 C). After the discharge at 5 C, the discharge capacity of the PPy coated caddice-clew-like MnO$_2$ sample is 508 mAh g^{-1} at 0.2 C, while much smaller discharge capacity is obtained as only 160 mAh g^{-1} at 0.2 C of the bare caddice-clew-like MnO$_2$ sample. So, the PPy-coated caddice-clew-like MnO$_2$ sample has improved rate performance. The situation of the PPy-coated urchin-like MnO$_2$ sample is much similar; nevertheless, the discharge capacity is a little lower than that of the PPy-coated caddice-clew-like MnO$_2$ sample.

As shown in the rate performance, the urchin-like MnO$_2$ micromaterial has relatively higher discharge specific capacity than caddice-clew-like MnO$_2$ micromaterial, which is consistent with previous reports [14]. However, after PPy coating, the caddice-clew-like MnO$_2$@PPy sample has better lithium-storage cyclic stability. Here, the conjugate degree of the PPy may be one

reason. The FT-IR analysis indicates that the PPy conjugate degree of the caddice-clew-like MnO$_2$@PPy sample is higher. So, the caddice-clew-like MnO$_2$@PPy sample should have better conductivity and better electrochemical performance. To confirm it, the EIS tests are carried out.

Figure 8 presents the EIS results for lithium cells after the fifth cycle at an ope-circuit voltage. As shown in Fig. 8a, the impedance spectra of caddice-clew-like MnO$_2$ obviously consists of two oblate semicircles in the high-to-medium-frequency region and an inclined line in the low-frequency region. However, the two semicircles of the other three samples are not easily distinguishable. An intercept at the Z_{real} axis in the high-frequency region corresponds to the ohmic electrolyte resistance (R_s). The first semicircle in the high frequency ascribes to the Li-ion migration resistance (R_{sf}) through the SEI films. The second semicircle in the high-to-medium frequency ascribes to the charge transfer resistance (R_{ct}). The inclined line at low-frequency region represents the Warburg impedance (W_s), which is associated with

Feng et al. Nanoscale Research Letters (2017) 12:518

Page 9 of 10

Fig. 8 Nyquist plot of Li/MnO$_2$ cells at open-circuit voltage. (**a**) caddice-clew-like MnO$_2$ sample. (**b**) Urchin-like MnO$_2$ sample. (**c**) 50 μL PPy-coated caddice-clew-like MnO$_2$ sample. (**d**) 30 μL PPy-coated urchin-like MnO$_2$ sample

lithium-ion diffusion in the active material. The semicircular parts of both the hybrid MnO$_2$@PPy samples are much smaller than that of the uncoated MnO$_2$ sample. This indicates that the conductivities of the hybrid MnO$_2$@PPy samples are better and the charge transfer resistance of Li ion decreases after PPy coating. The semicircle resistance of caddice-clew-like MnO$_2$@PPy sample is only 77 Ω. The semicircle resistance of urchin-like MnO$_2$@PPy sample is only 95 Ω. Here, after PPy coating, the lower resistance of caddice-clew-like MnO$_2$ micromaterial can explain the better lithium-storage cyclic stability.

Conclusions

In summary, MnO$_2$@PPy core-shell micromaterials are successfully prepared by chemical polymerization of pyrrole on the MnO$_2$ surface. The thickness of the PPy shell can be adjusted by the usage of pyrrole. After formation of MnO$_2$@PPy core-shell micromaterials, the cyclic performances as an anode for lithium-ion batteries are improved. Fifty microliters of PPy-coated caddice-clew-like MnO$_2$ has the best cyclic performances and has 620 mAh g^{-1} discharge specific capacities after 300 cycles. As a comparison, the discharge specific capacity of bare MnO$_2$ materials falls below 200 mAh g^{-1} after 10 cycles. The improved lithium-storage cyclic stability of the MnO$_2$@PPy samples can attribute to the core-shell hybrid structure. In this structure, the flexible PPy shell can effectively buffer the structural expansion and contraction of MnO$_2$ caused by the repeated embedding and disengagement of Li ions and can prevent the pulverization of MnO$_2$. Therefore, this experiment of PPy coating provides us an effective way to mitigate the problem of capacity fading of the transition metal oxide materials as anode materials for LIBs.

Additional file

Additional file 1: Supporting information. (DOC 3297 kb)

Authors' Contributions
The experiments and characterization presented in this work were carried out by LF, ZX, YZ, and RW. The experiments were designed by LF. The experiments were discussed in the results by LF, Y Z, WB, SJ JY, ZZ, and HG. All authors read and approved the final manuscript.

Competing Interests
The authors declare that they have no competing interests.

Publisher's Note
Springer Nature remains neutral with regard to jurisdictional claims in published maps and institutional affiliations.

References
1. Poizot P, Laruelle S, Grugeon S, Dupont L, Tarascon JM (2000) Nano-sized transition-metaloxides as negative-electrode materials for lithium-ion batteries. Nature 407:496–499
2. Zhang J, Yu A (2016) Nanostructured transition metal oxides as advanced anodes for lithium-ion batteries. Sci Bull 60:823–838
3. Xu JS, Zhu YJ (2012) Monodisperse Fe$_3$O$_4$ and γ-Fe$_2$O$_3$ magnetic mesoporous microspheres as anode materials for lithium-ion batteries. ACS Appl Mater Interfaces 4:4752–4757
4. Wu H, Wang Y, Zheng C, Zhu J, Wu G, Li X (2016) Multi-shelled NiO hollow spheres: easy hydrothermal synthesis and lithium storage performances. J Alloys Compd 685:8–14
5. Wang Z, Qu S, Cheng Y, Zheng C, Chen S, Wu H (2017) Facile synthesis of Co$_3$O$_4$ spheres and their unexpected high specific discharge capacity for Lithium-ion batteries. Appl Surf Sci 416:338–343
6. Wu G, Wu H, Wang K, Zheng C, Wang Y, Feng A (2016) Facile synthesis and application of multi-shelled SnO$_2$ hollow spheres in lithium ion battery. RSC Adv 6:58069–58076
7. Li B, Rong G, Xie Y, Huang L, Feng C (2006) Low-temperature synthesis of γ-MnO$_2$ hollow urchins and their application in rechargeable Li$^+$ batteries. Inorg Chem 45:6404–6410
8. Gu X, Yue J, Li L, Xue H, Yang J, Zhao X (2015) General synthesis of MnOx (MnO$_2$, Mn$_2$O$_3$, Mn$_3$O$_4$, MnO) hierarchical microspheres as lithium-ion battery anodes. Electrochim Acta 184:250–256
9. Liu X, Piao J, Bin D, Zhang T, Duan S, Wu Z, Cao A, Wan L (2017) Controlled formation of uniform nanoshells of manganese oxide and their potential in lithium ion batteries. Chem Commun 53:2846–2849
10. Liu H, Hu Z, Ruan H, Hu R, Su Y, Zhang L, Zhang J (2016) Nanostructured MnO$_2$ anode materials for advanced lithium ion batteries. J Mater Sci Mater Electron 27:11541–11547
11. Zhao J, Tao Z, Liang J, Chen J (2008) Facile synthesis of nanoporous γ-MnO$_2$ structures and their application in rechargeable Li-ion batteries. Cryst Growth Des 8:2799–2805
12. Cheng F, Zhao J, Song W, Li C, Ma H, Chen J, Shen P (2006) Facile controlled synthesis of MnO$_2$ nanostructures of novel shapes and their application in batteries. Inorg Chem 45:2038–2044

Feng *et al. Nanoscale Research Letters* (2017) 12:518

Page 10 of 10

13. Zhang K, Han X, Hu Z, Zhang X, Tao Z, Chen J (2015) Nanostructured Mn-based oxides for electrochemical energy storage and conversion. Chem Soc Rev 44:699–728

14. Feng L, Xuan Z, Zhao H, Bai Y, Guo J, Su C (2014) MnO_2 prepared by hydrothermal method and electrochemical performance as anode for lithium-ion battery. Nanoscale Res Lett 9:290

15. Chen X, Zhang N, Sun K (2011) 3d transition-metal oxides as anode micro/nano-materials for lithium ion batteries. Process Chem (Chin) 23:2045–2054

16. Feng L, Su C, Xuan Z, Guo J, Zhang Y (2013) Recent progress in metal oxide based materials as anode materials for lithium- ion batteries. Nano Biomed Eng 5:57–64

17. Mao W, Ai G, Dai Y, Fu Y, Ma Y, Shi S, Soe R, Zhang X, Qu D, Tang Z, Battaglia VS (2016) In-situ synthesis of MnO_2@CNT microsphere composites with enhanced electrochemical performances for lithium-ion batteries. J Power Sources 310:54–60

18. Zou BK, Zhang YY, Wang JY, Liang X, Ma XH, Chen CH (2015) Hydrothermally enhanced MnO/reduced graphite oxide composite anode materials for high performance lithium-ion batteries. Electrochim Acta 167:25–31

19. Yin Z, Fan W, Ding Y, Li J, Guan L, Zheng Q (2015) Shell structure control of PPy-modified CuO composite nanoleaves for lithium batteries with improved cyclic performance. ACS Sustain Chem Eng 3:507–517

20. Li L, Raji ARO, Tour JM (2013) Graphene-wrapped MnO_2—graphene nanoribbons as anode materials for high-performance lithium ion batteries. Adv Mater 25:6298–6302

21. Yu P, Zhang X, Wang D, Wang L, Ma Y (2009) Shape-controlled synthesis of 3D hierarchical MnO_2 nanostructures for electrochemical supercapacitors. Cryst Growth Des 9:528–533

22. Gangopadhyay R, De A (1999) Polypyrrole-ferric oxide conducting nanocomposites, 1. Synthesis and characterization. Eur Polym J 35:1985–1992

23. Cui L, Shen J, Cheng F, Tao Z, Chen J (2011) SnO_2 nanoparticles@polypyrrole nanowires composite as anode materials for rechargeable lithium-ion batteries. J Power Sources 196:2195–2201

24. Idris NH, Wang J, Chou S, Zhong C, Rahman MM, Liu H (2011) Effects of polypyrrole on the performance of nickel oxide anode materials for rechargeable lithium-ion batteries. J Mater Res 26:860–866

25. Yuan L, Wang J, Chew SY, Chen J, Guo ZP, Zhao L, Konstantinov K, Liu HK (2007) Synthesis and characterization of SnO_2-polypyrrole composite for lithium-ion battery. J Power Sources 174:1183–1187